Analysis of the slip coefficient and defect velocity in the Knudsen layer of a rarefied gas using the linearized moment equations

Xiao-Jun Gu,* David R. Emerson, and Gui-Hua Tang†
Computational Science and Engineering Department, STFC Daresbury Laboratory, Warrington WA4 4AD, United Kingdom
(Received 9 September 2009; published 19 January 2010)

The linearized R13 and R26 moment equations are used to study Kramers' problem. Analytical solutions for the defect velocity and slip coefficient are derived and compared with numerical results from the kinetic theory. It is found that the linearized R26 equations can capture the Knudsen layer fairly accurately in terms of the defect velocity and slip coefficient, while the linearized R13 equations underpredict the kinetic data. At the wall, however, the kinetic models predict a slightly higher value for the defect velocity than the linearized R26 equations. In general, the linearized R26 equations perform well for both specular and diffusive walls.

DOI: 10.1103/PhysRevE.81.016313 PACS number(s): 47.10.ab, 51.10.+y, 47.45.Gx

I. INTRODUCTION

The state of a dilute gas can be described by either kinetic theory or hydrodynamics. In kinetic theory, the gas is treated as a large number of interacting molecules that undergo binary collisions and the particles rebound according to prescribed laws [1,2]. In contrast, the hydrodynamic equations govern the macroscopic behavior of the gas. When the number of collisions between the gas molecules is sufficiently large for a gas to reach a statistically steady (equilibrium) state, the molecular distribution function can be represented by the Maxwellian parametrized by traditional hydrodynamic variables. These macroscopic quantities are governed by the traditional hydrodynamic Navier-Stokes-Fourier (NSF) equations. However, the molecular distribution will deviate from the Maxwellian when the gas is in a nonequilibrium state and the NSF equations are no longer accurate or valid [3]. Directly solving the Boltzmann equation for practical applications remains formidable due to the complicated structure of the collision term and its high dimensionality. It is also computationally expensive to use numerical approaches, such as the direct simulation Monte Carlo methods, in a regime not far from the equilibrium state. This is particularly true for the low-speed flows encountered in micro-electro-mechanical systems. Alternative macroscopic modeling and simulation strategies [4–10] have been developed over many years; among them, the method of moments is now showing great potential for solving real applications.

The method of moments was originally proposed by Grad [9] as an approximate solution procedure to Boltzmann's equation. It was initially used to study hyperbolic flows such as shock structure [11]. The Grad-type 13 and 26 moment field equations have also been applied to wall-bounded geometries, such as planar Couette flow, to investigate the gas-wall interaction effect on the gas state [12,13]. It was found that Grad's original method cannot capture the Knudsen layer very well. Significant effort and progress have been made in recent years, particularly, the introduction of regularization [14] and the treatment of solid boundaries [15,16]. Recent studies have shown that both the regularized 13 (R13) and 26 (R26) moment equations are able to capture several well-known nonequilibrium phenomena such as the bimodal temperature profile in force-driven Poiseuille flow, nongradient heat flux in Couette flow, and the Knudsen minimum [15–20]. However, in the transition regime, where the flow is dominated by Knudsen layers, the R13 equations are unable to provide an accurate description of the near-wall velocity [17–20]. This is because the Knudsen layer appears as superpositions of exponential layers [21]. The R13 equations are the lowest moment system that can describe both gradient and nongradient transport modes in the transition regime, but they can provide only one exponential layer to describe the velocity in the Knudsen layer [20]. In contrast, the R26 equations provide two exponential layers to describe the velocity close to the wall, which provides a significant improvement in accuracy [18,22].

For many low speed flows, it should be sufficient to use a linearized set of moment equations. In the present study, both the linearized R13 (LR13) and R26 (LR26) equations are used to study the flow behavior in the early transition regime. Kramers' problem is the most basic configuration, where the effect of a solid boundary can be investigated without the additional complications found in more realistic geometries. This problem has been extensively studied [23–27] and it provides a useful benchmark for the development of macroscopic models. In this paper, analytical solutions of Kramers' problem are obtained from the LR13 and LR26 moment equations and the defect velocity and slip coefficient are compared with numerical solutions from the kinetic theory to assess the validity and accuracy of the moment equations. We will show that rarefaction effects can be described by the macroscopic governing equations to good accuracy and the physics of nonequilibrium gas flow is well embedded in the moment equations in the early transition regime.

II. LINEARIZED MOMENT EQUATIONS AND THE SOLUTION OF KRAMERS' PROBLEM

The moment method provides a bridge between kinetic theory and hydrodynamics and extends classical fluid dy-

*Corresponding author. FAX: + 44 (0) 1925 603 634; xiaojun.gu@stfc.ac.uk
†Present address: School of Energy and Power Engineering, State Key Lab of Multiphase Flow, Xi'an Jiaotong University, Xi'an 710049, China.

namics to nonequilibrium flow. Once the distribution function f is known, the moments with respect to the particle's velocity $\boldsymbol{\xi}$ can be determined. For example, the density ρ and the momentum ρu_i can be obtained from $\rho=\int f d\boldsymbol{\xi}$ and $\rho u_i = \int \xi_i f d\boldsymbol{\xi}$, where ξ_i and u_i represent the particle and fluid velocity, respectively. It is convenient to introduce the intrinsic or peculiar velocity as $c_i=\xi_i-u_i$, so that the moments with respect to c_i can be conveniently calculated. A set of N moments are then used to describe the state of the gas through $\rho_{i_1 i_2 \ldots i_N}=\int c_{i_1} c_{i_2} \ldots c_{i_N} f d\boldsymbol{\xi}$.

Any moment can be expressed by its trace and traceless part [5,6]. For example, the pressure tensor can be separated as $p_{ij}=\int c_i c_j f d\boldsymbol{\xi}=p\delta_{ij}+p_{\langle ij\rangle}=p\delta_{ij}+\sigma_{ij}$, where δ_{ij} is the Kronecker delta function, $p=p_{kk}/3$ is the pressure, and $\sigma_{ij}=p_{\langle ij\rangle}$ is the deviatoric stress tensor. The angular brackets are used to denote the traceless part of a symmetric tensor [6]. Furthermore, the thermal energy density ε is given by $\rho\varepsilon = \int c_k c_k f d\boldsymbol{\xi}/2=3\rho RT/2$. Here $R=k_B/m$ is the gas constant, k_B is Boltzmann's constant, and m is the mass of a molecule. The temperature T is related to the pressure and density by the ideal-gas law $p=\rho RT$, and the heat flux vector is defined as $q_i=\int c_k c_k c_i f d\boldsymbol{\xi}/2$.

In Grad's approach [9], the molecular distribution function is expanded in terms of Hermite polynomials; the coefficients of which are linear combinations of the moments of the distribution function. An infinite set of Hermite coefficients is equivalent to the distribution function itself and there is no loss of any kinetic information. In practice, however, the distribution function has to be truncated, and the specific problem to be addressed will determine the order of the truncation. The truncated distribution will be denoted as Grad's distribution function f_G.

For the convenience of modeling, the high moments are decomposed into values approximated with Grad's distribution function $\rho_{i_1 i_2,\ldots,i_N}|_{f_G}$ and the deviation from their true value. With Grad's 26 moment distribution function f_{G26}, the following high moments used in the present study can be expressed by

$$\rho_{\langle ijk\rangle} = m_{ijk} + \rho_{\langle ijk\rangle|f_{G26}} = m_{ijk},$$

$$\rho_{\langle ijkl\rangle} = \phi_{ijkl} + \rho_{\langle ijkl\rangle|f_{G26}} = \phi_{ijkl},$$

$$\rho_{\langle ij\rangle rr} = R_{ij} + \rho_{\langle ij\rangle rr|f_{G26}} = R_{ij} + 7RT\sigma_{ij},$$

$$\rho_{rr\langle ijk\rangle} = \psi_{ijk} + \rho_{rr\langle ijk\rangle|f_{G26}} = \psi_{ijk} + 9RTm_{ijk},$$

$$\rho_{rrss} = \Delta + \rho_{rrss|f_{G26}} = \Delta + 15pRT,$$

$$\rho_{rrssi} = \Omega_i + \rho_{rrssi|f_{G26}} = \Omega_i + 28RTq_i, \tag{1}$$

where m_{ijk}, R_{ij}, Δ, ψ_{ijk}, ϕ_{ijkl}, and Ω_i represent the difference between the true value of the higher moments and their corresponding approximation with f_{G26}.

The governing equations for the moments can be readily obtained from Boltzmann's equation [6]. The derivation of the R13 and R26 moment equations for monatomic gas of Maxwell molecules and their linearization can be found in Refs. [14,18,20,22], respectively. For Kramers' problem, the coordinates are chosen such that the wall is parallel to the x direction and y is the direction perpendicular to the wall which is located at $y=0$. The velocity in the x direction is u and the velocity in all other directions is zero. All derivatives in the x direction are zero and the mass conservation law is satisfied automatically. The linearized one-dimensional moment equations are decoupled into a velocity-related and temperature-related set. The equations involved in the velocity problem, obtained from the LR26 moment system, are reduced to a five moment system [22] for Maxwell molecules,

$$\frac{d\bar{\sigma}_{xy}}{d\bar{y}} = 0, \tag{2}$$

$$\frac{d\bar{m}_{xyy}}{d\bar{y}} = -\sqrt{\frac{\pi}{2}}\frac{L}{\lambda}\bar{\sigma}_{xy} - \frac{d\bar{u}}{d\bar{y}} - \frac{2}{5}\frac{d\bar{q}_x}{d\bar{y}}, \tag{3}$$

$$\frac{d\bar{R}_{xy}}{d\bar{y}} = -\frac{4}{3}\sqrt{\frac{\pi}{2}}\frac{L}{\lambda}\bar{q}_x - 2\frac{d\bar{\sigma}_{xy}}{d\bar{y}}, \tag{4}$$

$$\frac{d\bar{\phi}_{xyyy}}{d\bar{y}} = -\frac{3}{2}\sqrt{\frac{\pi}{2}}\frac{L}{\lambda}\bar{m}_{xyy} - \frac{8}{5}\frac{d\bar{\sigma}_{xy}}{d\bar{y}} - \frac{8}{35}\frac{d\bar{R}_{xy}}{d\bar{y}}, \tag{5}$$

$$\frac{d\bar{\psi}_{xyy}}{d\bar{y}} = -\frac{7}{6}\sqrt{\frac{\pi}{2}}\frac{L}{\lambda}\bar{R}_{xy} - \frac{14}{5}\frac{d\bar{q}_x}{d\bar{y}} - 2\frac{d\bar{m}_{xyy}}{d\bar{y}} - \frac{1}{5}\frac{d\bar{\Omega}_x}{d\bar{y}}, \tag{6}$$

closed by the following constitutive relationships:

$$\bar{\phi}_{xyyy} = -\frac{15}{7Z}\sqrt{\frac{2}{\pi}}\frac{\lambda}{L}\frac{d\bar{m}_{xyy}}{d\bar{y}}, \quad \bar{\psi}_{xyy} = -\frac{72}{35Y}\sqrt{\frac{2}{\pi}}\frac{\lambda}{L}\frac{d\bar{R}_{xy}}{d\bar{y}},$$

$$\bar{\Omega}_x = -4\sqrt{\frac{2}{\pi}}\frac{\lambda}{L}\frac{d\bar{R}_{xy}}{d\bar{y}}, \tag{7}$$

in which, $Y=1.698$ and $Z=2.097$ are collision constants for Maxwell molecules and L is a characteristic length. The variables with an overbar symbol are small dimensionless deviations from an equilibrium state given by ρ_o, T_o (or p_o), and u_o as defined in

$$u = \sqrt{RT_o}\bar{u}, \quad m_{xyy} = \rho_o (RT_o)^{3/2}\bar{m}_{xyy}, \quad \psi_{xyy} = \rho_o (RT_o)^{5/2}\bar{\psi}_{xyy},$$

$$\sigma_{xy} = \rho_o RT_o\bar{\sigma}_{xy}, \quad R_{xy} = \rho_o (RT_o)^2\bar{R}_{xy}, \quad \Omega_x = \rho_o (RT_o)^{5/2}\bar{\Omega}_x,$$

$$q_x = \rho_o (RT_o)^{3/2}\bar{q}_x, \quad \phi_{xyyy} = \rho_o (RT_o)^2\bar{\phi}_{xyyy}, \quad y = L\bar{y}. \tag{8}$$

The wall boundary conditions constructed from Maxwell's kinetic boundary treatment are [22]

$$\bar{u}_\tau = -\alpha^*\sqrt{\frac{\pi}{2}}\bar{\sigma}_{xy} - \frac{5\bar{m}_{xyy}+2\bar{q}_x}{10} + \frac{9\bar{\Omega}_x+70\bar{\psi}_{xyy}}{2520}, \tag{9}$$

$$\bar{q}_x = -\frac{5}{18}\alpha^* \sqrt{\frac{\pi}{2}}(7\bar{\sigma}_{xy} + \bar{R}_{xy}) - \frac{5\bar{u}_\tau}{3} - \frac{10\bar{m}_{xyy}}{9} - \frac{5\bar{\psi}_{xyy}}{81} - \frac{\bar{\Omega}_x}{56}, \tag{10}$$

$$\bar{m}_{xyy} = -\alpha^* \sqrt{\frac{\pi}{2}}\left(\bar{\sigma}_{xy} + \frac{\bar{R}_{xy}}{7} + \frac{\bar{\phi}_{xyyy}}{3}\right) - \frac{2}{5}\bar{q}_x - \frac{2\bar{u}_\tau}{3} - \frac{\bar{\psi}_{xyy}}{18} - \frac{\bar{\Omega}_x}{140}, \tag{11}$$

where $\alpha^* = (2-\alpha)/\alpha$ and α is the momentum accommodation coefficient, indicating that a fraction α of gas molecules will be diffusely reflected with a Maxwellian at the wall temperature, and the remaining fraction will undergo specular reflection. The slip velocity is u_τ and Eq. (9) is similar to the slip velocity boundary condition for the NSF equations with extra terms providing higher-order corrections [19]. For Kramers' problem, it is convenient to choose the mean free path defined by $\lambda = (\mu/p_o)\sqrt{\pi R T_o/2}$, as the characteristic length so that $\lambda/L = 1$.

Equation (2) indicates that the shear stress $\bar{\sigma}_{xy}$ is a constant in the whole domain. Integration of Eq. (3) gives the velocity as

$$\bar{u} = -\sqrt{\pi/2}\bar{\sigma}_{xy}\bar{y} - 2\bar{q}_x/5 - \bar{m}_{xyy} + A, \tag{12}$$

where A is an integration constant. The superposition of the velocity contributions from σ_{xy}, m_{xyy}, and q_x are clearly expressed by Eq. (12). This is an important feature that is not present in the NSF equations. The expressions for $\bar{q}_x$, $\bar{m}_{xyy}$, and $\bar{R}_{xy}$ can be obtained from Eqs. (4)–(7) as

$$\bar{m}_{xyy} = \sqrt{\pi/2}\bar{\sigma}_{xy}[C_1 e^{-(1.265\sqrt{\pi/2})\bar{y}} + C_2 e^{-(0.5102\sqrt{\pi/2})\bar{y}}], \tag{13}$$

$$\bar{q}_x = \sqrt{\pi/2}\bar{\sigma}_{xy}[-0.4435 C_1 e^{-(1.265\sqrt{\pi/2})\bar{y}} + 4.0491 C_2 e^{-(0.5102\sqrt{\pi/2})\bar{y}}], \tag{14}$$

$$\bar{R}_{xy} = \sqrt{\pi/2}\bar{\sigma}_{xy}[-0.4674 C_1 e^{-(1.265\sqrt{\pi/2})\bar{y}} + 10.5817 C_2 e^{-(0.5102\sqrt{\pi/2})\bar{y}}], \tag{15}$$

where C_1 and C_2 are integration constants. In the above solutions, the boundary condition that, as $\bar{y} \to \infty$, $\bar{q}_x$, $\bar{m}_{xyy}$, and $\bar{R}_{xy}$ will remain finite, has been used to remove the other two integration constants and the terms associated with them. The remaining integration constants A, C_1, and C_2 are determined from the wall boundary conditions (9)–(11) by

$$A = -\sqrt{\pi/2}\bar{\sigma}_{xy}(\alpha^* - 0.383 C_1 - 1.5686 C_2), \tag{16}$$

$$C_1 = -\alpha^* \frac{0.81265 \times 10^{-1}\alpha^2 + 1.2824\alpha}{0.48517 \times 10^{-2}\alpha^2 + 0.64884\alpha + 8.0995}, \tag{17}$$

$$C_2 = -\alpha^* \frac{0.8565 \times 10^{-3}\alpha^2 + 0.362\alpha}{0.48517 \times 10^{-2}\alpha^2 + 0.64884\alpha + 8.0995}. \tag{18}$$

Inserting Eqs. (13), (14), and (16) into Eq. (12), the final expression for velocity from the LR26 moment equations reads as

$$\bar{u} = -\sqrt{\pi/2}\bar{\sigma}_{xy}\bar{y} - \sqrt{\pi/2}\bar{\sigma}_{xy}(\alpha^* - 0.383 C_1 - 1.5686 C_2) - \sqrt{\pi/2}\bar{\sigma}_{xy}[0.8226 C_1 e^{-(1.265\sqrt{\pi/2})\bar{y}} + 2.6196 C_2 e^{-(0.5102\sqrt{\pi/2})\bar{y}}]. \tag{19}$$

In the LR13 system, the governing differential equations (5) and (6) are replaced by the following constitutive relationships [28]:

$$\bar{m}_{xyy} = -\frac{16}{15}\sqrt{\frac{2}{\pi}}\frac{d\bar{\sigma}_{xy}}{d\bar{y}}, \quad \bar{R}_{xy} = -\frac{12}{5}\sqrt{\frac{2}{\pi}}\frac{d\bar{q}_x}{d\bar{y}}, \tag{20}$$

along with the boundary conditions (9) and (10) without the higher moments $\bar{\psi}_{xyy}$ and $\bar{\Omega}_x$. For Kramers' problem, the velocity field for the LR13 equations is readily obtained as

$$\bar{u} = -\sqrt{\frac{\pi}{2}}\bar{\sigma}_{xy}\bar{y} - \alpha^*\sqrt{\frac{\pi}{2}}\bar{\sigma}_{xy}\left(\frac{13 + 2\alpha^*\sqrt{10\pi}}{12 + 2\alpha^*\sqrt{10\pi}}\right) + \alpha^*\sqrt{\frac{\pi}{2}}\bar{\sigma}_{xy}\left[\frac{e^{-(\sqrt{5\pi/18})\bar{y}}}{6 + \alpha^*\sqrt{10\pi}}\right]. \tag{21}$$

If we compare Eqs. (19) and (21), we can see that the LR26 equations provide two exponentials to describe the Knudsen layer, while the LR13 equations only contain one exponential. Recently, the velocity field for the LR13 equations based on the Bhatnagar-Gross-Krook (BGK) model was obtained [29]. With the notation of the present study, the solution can be written as

$$\bar{u} = -\sqrt{\frac{\pi}{2}}\bar{\sigma}_{xy}\bar{y} - \alpha^*\sqrt{\frac{\pi}{2}}\bar{\sigma}_{xy}\left(\frac{13 + \alpha^*\sqrt{70\pi}}{12 + \alpha^*\sqrt{70\pi}}\right) + \alpha^*\sqrt{\frac{\pi}{2}}\bar{\sigma}_{xy}\left[\frac{2e^{(-(\sqrt{70\pi}/14)\bar{y})}}{12 + \alpha^*\sqrt{70\pi}}\right]. \tag{22}$$

Clearly the BGK and Maxwell molecule models will produce Knudsen layers with different widths.

III. DEFECT VELOCITY AND SLIP COEFFICIENT

In kinetic theory, the defect velocity and slip coefficient are often used to study how the wall affects the velocity profile [23–27]. To be consistent with the kinetic solutions obtained from the Boltzmann equation, a reference velocity $u_o = -\sigma_{xy}(\lambda/\mu) = -\bar{\sigma}_{xy}\sqrt{\pi R T_o/2}$ is used to scale the velocity, i.e.,

$$\tilde{u} = u/u_o = \bar{y} + (\alpha^* - 0.383 C_1 - 1.5686 C_2) + [0.8226 C_1 e^{-(1.265\sqrt{\pi/2})\bar{y}} + 2.6196 C_2 e^{-(0.5102\sqrt{\pi/2})\bar{y}}]. \tag{23}$$

A defect velocity u_d is defined by $u_d = \bar{y} + \zeta - \tilde{u}$, and the slip

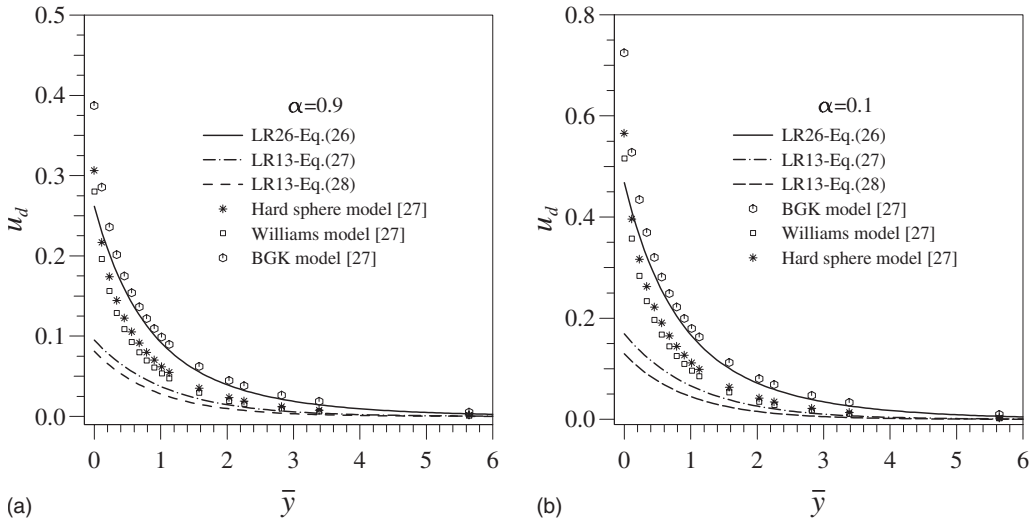

FIG. 1. Defect velocity profile for Kramers' problem: comparison between the moment equation solutions (lines) and kinetic theory (symbols) [27]. (Note: the original data in Ref. [27] are presented in terms of the mean free path defined by $l=(2/\sqrt{\pi})\lambda$. The data were converted to be consistent with the present definition of the mean free path λ.)

coefficient ζ is determined by $\lim_{\bar{y}\to\infty} u_d=0$ [24,27]. From the above condition, the expression of ζ for the LR26 moment equations can be written as

$$\zeta = \alpha^* - 0.383C_1 - 1.5686C_2 = \alpha^*\left(\frac{0.3732\times 10^{-1}\alpha^2 + 1.7078\alpha + 8.0995}{0.48517\times 10^{-2}\alpha^2 + 0.64884\alpha + 8.0995}\right) \quad (24)$$

and the defect velocity is expressed by

$$u_d = -0.8226C_1 e^{-(1.265\sqrt{\pi/2})\bar{y}} - 2.6196C_2 e^{-(0.5102\sqrt{\pi/2})\bar{y}}. \quad (25)$$

Similarly, we can obtain the defect velocity and slip coefficient for the LR13 equations, respectively, as

$$u_d = \alpha^*\left[\frac{e^{-(\sqrt{5\pi}/18)\bar{y}}}{6+\alpha^*\sqrt{10\pi}}\right],$$

$$\zeta = \alpha^*\left[\frac{(13-2\sqrt{10\pi})\alpha + 4\sqrt{10\pi}}{(12-2\sqrt{10\pi})\alpha + 4\sqrt{10\pi}}\right]. \quad (26)$$

For the LR13-BGK model [29], the defect velocity and slip coefficient, respectively, are

$$u_d = \alpha^*\left[\frac{2e^{[-(\sqrt{70\pi}/14)\bar{y}]}}{\sqrt{70\pi}\alpha^* + 12}\right],$$

$$\zeta = \alpha^*\left[\frac{(13-\sqrt{70\pi})\alpha + 2\sqrt{70\pi}}{(12-\sqrt{70\pi})\alpha + 2\sqrt{70\pi}}\right]. \quad (27)$$

IV. COMPARISON WITH KINETIC THEORY

In the work by Siewert [27], the Boltzmann equation was solved using three different kinetic models to determine the Knudsen layer velocity profile for Kramers' problem. These included the BGK model, the Williams model (the collision frequency is proportional to the magnitude of the velocity), and the hard-sphere model. Siewert investigated wall conditions, ranging from fully diffusive to specular-diffusive reflection. Figure 1 presents the analytical solutions of the defect velocity in the Knudsen layer from the moment equations in comparison with the computational results from the three kinetic models. For the case of $\alpha=0.9$, diffusive reflection from the wall dominates. The BGK kinetic model produces the largest defect velocity in the Knudsen layer, particularly close to the wall ($\bar{y}<0.5$). In contrast, the results from the Williams and hard-sphere models are in close agreement with each other. The analytical solution from the LR26 equations generally lies between the three models and, beyond $\bar{y}=0.5$, is in close agreement with the BGK model. However, at the wall, all kinetic models predict a higher defect velocity. Conversely, the solution obtained from the LR13 equations underpredicts the defect velocity significantly, as shown in Fig. 1(a). The solution of the LR13 equations based on the BGK model is also presented in Fig. 1. The difference between the two LR13 equation sets is not significant. As the LR13 system involves fewer equations and boundary conditions than the LR26 system, less kinetic information is preserved in the LR13 model. Clearly, the combination of two exponentials with different widths produces an improved Knudsen layer velocity profile. It is expected that more moments and their governing equations would generate more exponentials with different widths to fully recover the full kinetic information. As the value of the accommodation coefficient decreases, the previous observations remain valid although, as expected, the defect velocity increases, as shown in Fig. 1(b). In this case, where $\alpha=0.1$, specular wall reflection dominates. The results shown in Fig. 1 illustrate that the LR26 equations work well for walls exhibiting either diffusive or specular reflection.

Equation (12) illustrates that the velocity in the Knudsen layer consists of contributions from $\bar{\sigma}_{xy}$, $\bar{q}_x$, and $\bar{m}_{xyy}$. For the

LR13 equations, there is no mechanism for $\bar{m}_{xyy}$ to contribute; so the Knudsen layer is derived solely from the tangential heat flux $\bar{q}_x$. In the NSF system, $\bar{q}_x$ and $\bar{m}_{xyy}$ are not present, so there is no Knudsen layer. If we take the distance to the wall as the characteristic length, the corresponding Knudsen number is the reciprocal of $\bar{y}$. Figure 1 suggests that the LR26 and LR13 equations can capture the Knudsen layer velocity in a half-space configuration for a Knudsen number equal to 2 ($\bar{y}=0.5$) and 0.5 ($\bar{y}=2$), respectively. However, in confined geometries, Knudsen layers from opposite walls will overlap [18] and, for the R26 and R13 equations, this will reduce the value of the Knudsen number to 1 and 0.2, respectively. These results provide a clear indication that the higher moment equations can be used in the early transition regime with good accuracy.

A further test of the ability of macroscopic models to accurately capture the nonequilibrium features in the Knudsen layer is an evaluation of the slip coefficient. If we plot ζ against α, Eqs. (24), (26), and (27) will lie on different curves but will be so close to each other that the differences between them cannot be shown in the figure because of the large plotting scale. It then gives the impression that they produce the same value of the slip coefficient and researchers could draw wrong conclusions from such a plot that the NSF equations can produce the same slip coefficient as the BGK kinetic equation [29]. In fact, at $\alpha=1$, the LR26 gives $\zeta=1.1247$, the LR13 in Eq. (26) gives $\zeta=1.0431$, the LR13 in Eq. (27) gives $\zeta=1.0372$, and the NSF gives $\zeta=1$. It is well known that the slip coefficient for the kinetic BGK equation is 1.1466 at $\alpha=1$. The large plotting scale comes from the factor α^* in Eqs. (24), (26), and (27). To gain a better understanding of the accuracy of each equation set against kinetic data, it is more appropriate to plot ζ/α^* against α, as shown in Fig. 2, where we compare our results with those from kinetic theory [27]. The NSF equations always give $\zeta/\alpha^*=1$. The slip coefficient predicted by the BGK model is greater than the value from either the Williams or hard-sphere models, and the solution from the LR26 equations lies between them. In contrast, both LR13 solutions underestimate the value of the slip coefficient due to the information lost in the reduction in the moment equations. The slip coefficient is often used in the slip boundary condition for the NSF equations to compensate for their inability to describe Knudsen layers. However, the value of the slip coefficient determined from Kramers' problem depends on the kinetic model used and might only be applicable to planar geometry. In complex geometries and flow conditions, care must be taken when using a slip coefficient in NSF calculations.

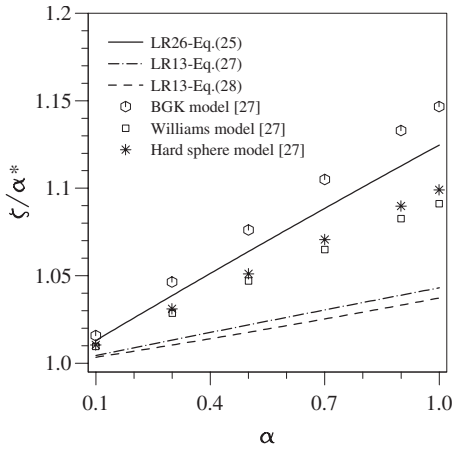

FIG. 2. Analysis of the slip coefficient: comparison between the moment equation solutions (lines) and kinetic theory (symbols) [27]. (Note: the original data in Ref. [27] are presented in terms of the mean free path defined by $l=(2/\sqrt{\pi})\lambda$. The data were converted to be consistent with the present definition of the mean free path λ.)

V. CONCLUSIONS

The moment method is employed to study Kramers' problem. Analytical solutions for the defect velocity and slip coefficient have been obtained for the LR13 and LR26 moment equations, respectively. In comparison with data from kinetic theory, it is found that the LR26 equations are able to describe the Knudsen layer fairly accurately in terms of the defect velocity and the slip coefficient, while the LR13 equations consistently underpredict the kinetic data. The wall boundary conditions for the R26 equations are valid for walls dominated by either specular or diffusive reflection, and the results indicate that the physics of nonequilibrium gas flow can be captured by high-order moment equations.

ACKNOWLEDGMENT

The authors would like to thank the Engineering and Physical Science Research Council (EPSRC) for their support of Collaborative Computational Project 12 (CCP12).

[1] C. Cercignani, *The Boltzmann Equation and Its Applications* (Springer, New York, 1988).
[2] G. Bird, *Molecular Gas Dynamics and the Direct Simulation of Gas Flows* (Clarendon Press, Oxford, 1994).
[3] M. Gad-el-Hak, ASME Trans. J. Fluids Eng. **121**, 5 (1999).
[4] S. Chapman and T. G. Cowling, *The Mathematical Theory of Non-uniform Gases* (Cambridge University Press, Cambridge, 1970).
[5] I. Müller and T. Ruggeri, *Extended Thermodynamics*, 2nd ed. (Springer, New York, 1993).
[6] H. Struchtrup, *Macroscopic Transport Equations for Rarefied Gas Flows* (Springer-Verlag, Berlin, 2005).
[7] K. Xu, J. Comput. Phys. **171**, 289 (2001).
[8] X. Shan, X.-F. Yuan, and H. Chen, J. Fluid Mech. **550**, 413 (2006).
[9] H. Grad, Commun. Pure Appl. Math. **2**, 331 (1949).
[10] C. D. Levermore, J. Stat. Phys. **83**, 1021 (1996).
[11] H. Grad, Commun. Pure Appl. Math. **5**, 257 (1952).

[12] W. Marques and G. M. Kremer, Continuum Mech. Thermodyn. **13**, 207 (2001).
[13] D. Reitebuch and W. Weiss, Continuum Mech. Thermodyn. **11**, 217 (1999).
[14] H. Struchtrup and M. Torrilhon, Phys. Fluids **15**, 2668 (2003).
[15] X. J. Gu and D. R. Emerson, J. Comput. Phys. **225**, 263 (2007).
[16] M. Torrilhon and H. Struchtrup, J. Comput. Phys. **227**, 1982 (2008).
[17] X. J. Gu, R. W. Barber, and D. R. Emerson, Nanoscale Microscale Thermophys. Eng. **11**, 85 (2007).
[18] X. J. Gu and D. R. Emerson, J. Fluid Mech. **636**, 177 (2009).
[19] H. Struchtrup and M. Torrilhon, Phys. Rev. E **78**, 046301 (2008).
[20] P. Taheri, M. Torrilhon, and H. Struchtrup, Phys. Fluids **21**, 017102 (2009).
[21] H. Struchtrup, Physica A **387**, 1750 (2008).
[22] X. J. Gu, D. R. Emerson, and G. H. Tang, Continuum Mech. Thermodyn. **21**, 345 (2009).
[23] S. Albertoni, C. Cercignani, and L. Gotusso, Phys. Fluids **6**, 993 (1963).
[24] S. K. Loyalka, Phys. Fluids **18**, 1666 (1975).
[25] S. K. Loyalka and K. A. Hickey, Phys. Fluids A **1**, 612 (1989).
[26] S. K. Loyalka and R. V. Tompson, Eur. J. Mech. B/Fluids **28**, 211 (2009).
[27] C. E. Siewert, Eur. J. Appl. Math. **12**, 179 (2001).
[28] H. Struchtrup and M. Torrilhon, Phys. Rev. Lett. **99**, 014502 (2007).
[29] P. Taheri, A. S. Rana, M. Torrilhon, and H. Struchtrup, Continuum Mech. Thermodyn. **21**, 423 (2009).